Journal of Nuclear Materials 393 (2009) 369–380

Contents lists available at ScienceDirect

Journal of Nuclear Materials

journal homepage: www.elsevier.com/locate/jnucmat

Corrosion of the AlFeNi alloy used for the fuel cladding in the Jules Horowitz research reactor

M. Wintergerst [a,*], N. Dacheux [b], F. Datcharry [c], E. Herms [c], B. Kapusta [a]

[a] CEA-Saclay, DEN/DMN/SEMI/LCMI, 91191 Gif-sur-Yvette, France
[b] ICSM – Bat 426, Centre de Marcoule, University of Montpellier 2, BP 17171, 30207 Bagnols-sur-Cèze, France
[c] CEA-Saclay, DEN/DPC/SCCME/LECA, 91191 Gif-sur-Yvette, France

ARTICLE INFO

Article history:
Received 9 October 2008
Accepted 2 June 2009

ABSTRACT

The AlFeNi aluminium alloy (1 wt% Fe, 1 wt% Ni, 1 wt% Mg) is expected to be used as nuclear fuel cladding for the Jules Horowitz experimental reactor. To guarantee a safe behaviour of the fuel, a good understanding of the fuel clad corrosion mechanisms is required. In this field, the experimental characterization of the selected alloy was performed. Then experimental studies of the aluminium alloy corrosion product obtained in autoclaves have shown an oxide film composed of two layers. This duplex structure results from a mixed growth mechanism: an anionic growth to develop the inner oxide and a cationic diffusion parallel to a dissolution–precipitation process to form the outer zone. Dynamic experiments at 70 °C have demonstrated that a solid diffusion step controls the release kinetic. Then post-irradiation exams performed on irradiated fuel plates were used to investigate the effects of the irradiation on the corrosion behaviour in the reactor core.

1. Introduction

For the Jules Horowitz new material-testing Reactor (JHR), an aluminium alloy, called AlFeNi, will be used for the cladding of the nuclear fuel plates. This alloy (Al – 1 wt% Fe – 1 wt% Ni – 1 wt% Mg), already used as fuel cladding in two other experimental reactors, was developed on the basis of its good corrosion resistance in water at high temperatures. However, few studies dealing with the alteration processes in water and its relationships with irradiation effects have been performed on this alloy.

Moreover, the conception of the JHR fuel requires a better knowledge of the corrosion mechanisms. Indeed, high performances regarding allowed neutron fluences and better versatility for experimental facilities are expected for this reactor. To reach such performances, the design of the fuel assembly was strongly optimized. Its lifetime in the reactor and its properties regarding thermal–hydraulic conditions are strongly dependent on the development of an oxide scale up to the cladding surface. Due to its poor thermal properties, this neoformed oxide layer can modify the quality of the thermal exchanges with the coolant system. And a temperature rise of the fuel can impact on the fuel plate integrity through the acceleration of the clad corrosion or the decrease of the mechanical properties of the aluminium cladding at high temperatures. Both phenomena should induce a fuel clad failure with considerable issues.

Many oxide thickness prediction models [1–6] have been developed for out-of-pile data and in-pile tests and are based on empirical correlations between oxide film thicknesses and testing time. Nevertheless, their application ranges are limited to respective test conditions and can not be extrapolated. Moreover, even if there are usual power law models linked to diffusion of species, it is difficult to associate these laws with physical and chemical mechanisms.

To cool down the temperature of the clad, deionized water will be used in JHR. This is the reason why our study is specifically focused on the AlFeNi alloy corrosion by pure water.

After the complete characterization of the AlFeNi alloy, corrosion tests were performed in autoclaves and in an open-flow device on AlFeNi plates representative of the JHR fuel cladding. The last part of this paper deals with the post-irradiation exams performed on irradiated fuel plates in the Belgian BR2 reactor.

2. Characterization of the AlFeNi alloy

2.1. Experimental

The AlFeNi alloy has been developed during the fifties for nuclear fuel clad application [7,8]. The main goal was to increase the corrosion resistance of the material at high temperature (between 250 and 300 °C) for high fluxes reactors without decreasing the neutron adsorption performance of aluminium. The AlFeNi alloy is mainly composed by aluminium (~96 wt%), iron (1 wt%), nickel (1 wt%) and magnesium (1 wt%). The associated complete specifications are summarized in Table 1.

* Corresponding author. Tel.: +33 1 69 08 18 18; fax: +33 1 69 08 93 24.
E-mail address: matthieu.wintergerst@cea.fr (M. Wintergerst).

0022-3115/$ - see front matter © 2009 Elsevier B.V. All rights reserved.
doi:10.1016/j.jnucmat.2009.06.003

Table 1
Specified chemical composition of the AlFeNi aluminium alloy.

Element	Specification (wt%)
Fe	0.80–1.20
Ni	0.80–1.20
Fe + Ni	$\geqslant$1.80
Mg	0.80–1.20
Mn	0.20–0.60
Cr	0.20–0.50
Zr	0.06–0.14
Si	$\leqslant$0.30

For this study, we used four sorts of AlFeNi plates, depending on their metallurgical temper: cold work hardened (at 16% and 20%) or annealed at 425 °C for 2.5 h for 16% and 20% strain hardened plates. Provided by CERCA (Romans, France) to CEA, the four kinds of rolled 1.4 mm thick AlFeNi sheets are considered to be representative of the fuel cladding. The alloy samples characterized (20 × 20 mm) were cut from respective materials. Coupons were embedded in a conductive, Bakelite resin with carbon filler, and then polished with SiC paper. The microstructure was revealed by optical and Electron Microscopies (SEM and TEM). The chemical composition was obtained through ElectronProbe MicroAnalysis (EPMA) and Transmission Electron Microscopy (TEM).

2.2. Chemical characterization

The metallurgical behaviour of additional elements is different from one to the other. SEM and TEM observations (Fig. 1) demonstrate the presence of intermetallic precipitates inside the aluminium matrix.

Magnesium is in substitution in the face-centered cubic crystallographic structure (fcc α matrix) of aluminium. This point was demonstrated through EPMA quantifications and X-ray maps (Fig. 2) but also by X-ray diffraction (XRD) experiments (Fig. 3). Through X-ray mapping, the correlation between aluminium and magnesium is immediately visible. Moreover the lattice parameter of the AlFeNi matrix was evaluated by XRD to 4.0550 Å and compared to 4.0495 Å, known for pure aluminium. According to Ref. [9], aluminium α lattice parameter is not sensitive to element addition expect for magnesium, which is soluble in aluminium. Assuming a linear dependence of the lattice parameter with the magnesium content, the parameter shift calculated in the AlFeNi alloy corresponds to a magnesium content of 1.13 wt%, in agreement with the alloy specifications.

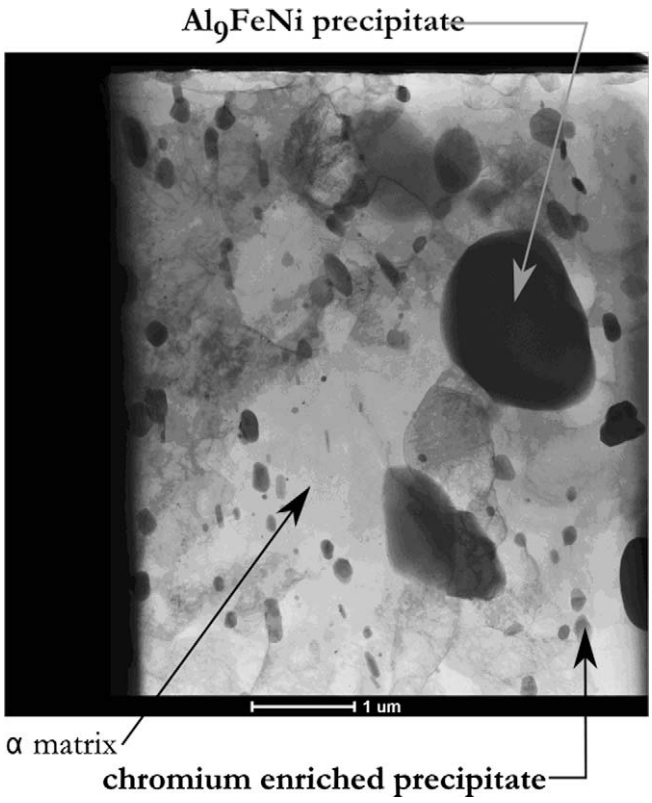

Fig. 1. Micrograph of the AlFeNi alloy, underscoring the intermetallic precipitation inside the α matrix.

Two kinds of precipitates have been characterized by TEM: respectively iron–nickel rich and chromium rich, insoluble intermetallic phases. Iron and nickel are in combination (X-ray maps of Fig. 2) and present as micrometric isotropic precipitates dispersed in the Al-Mg matrix. EPMA quantifications and EDX measurements led to a stoichiometry close to Al_9FeNi as expected from available references [8] (Fig. 4). Chromium enriched precipitates (between 3 and 6 wt% on Al based) of 200 nm diameter are also observed.

2.3. Metallurgical study of the AlFeNi alloy

A chloride acid attack was considered to reveal the metallurgical microstructure and grain size. The microstructure was then observed by optical microscopy. The grain size appears to be dependent on the annealing heat treatment. It is found to be very heterogeneous, but always stays relatively large, as shown in Table 2. According to the temper, the average grain size is ranging between 0.3 and 4.4 mm^2. The grain morphology also depends on the plate metallurgical state: on cold worked plates, grains are strongly oriented by rolling direction. After annealing at 425 °C, grains become equiaxed and the global decrease of the average size is associated to recrystallisation, as expected for an aluminium alloy [10,11] exposed to this temperature.

3. Characterization of the corrosion product of the AlFeNi alloy in autoclave

3.1. Experimental protocol

In order to characterize the corrosion products, static corrosion experiments were performed in autoclave (V = 5L – titanium) on fresh AlFeNi alloy plates (20 × 20 mm). Some experiments were carried out at 70, 165 and 250 °C for various exposure times (6–45 days). Pure deionized water was used for the experiments as representative of the coolant water in the JHR. The average pH of water, measured at room temperature before each test in the titanium autoclave, was at 6.9 with conductivity inferior to 1 μS cm^{-1}. Before corrosion tests, the exposed samples were polished with SiC paper. After corrosion, if necessary they were embedded in conductive resin and polished, then examined through SEM, FEG-SEM, TEM, EPMA, XRD and μ-Raman spectroscopy.

3.2. Description of the corrosion product

Micrographs show a duplex structure for the corrosion products (Fig. 5). In the first layer, close to the metal zone, the biggest precipitates of Al_9FeNi remained visible. The outer layer, in contact with the water is not so compact than the inner one and shows an apparent large porosity. Various techniques were used to characterize each zone.

Firstly, due to unknown reasons, many cracks are visible in the oxide film (Fig. 5). Various origins can be proposed to explain the

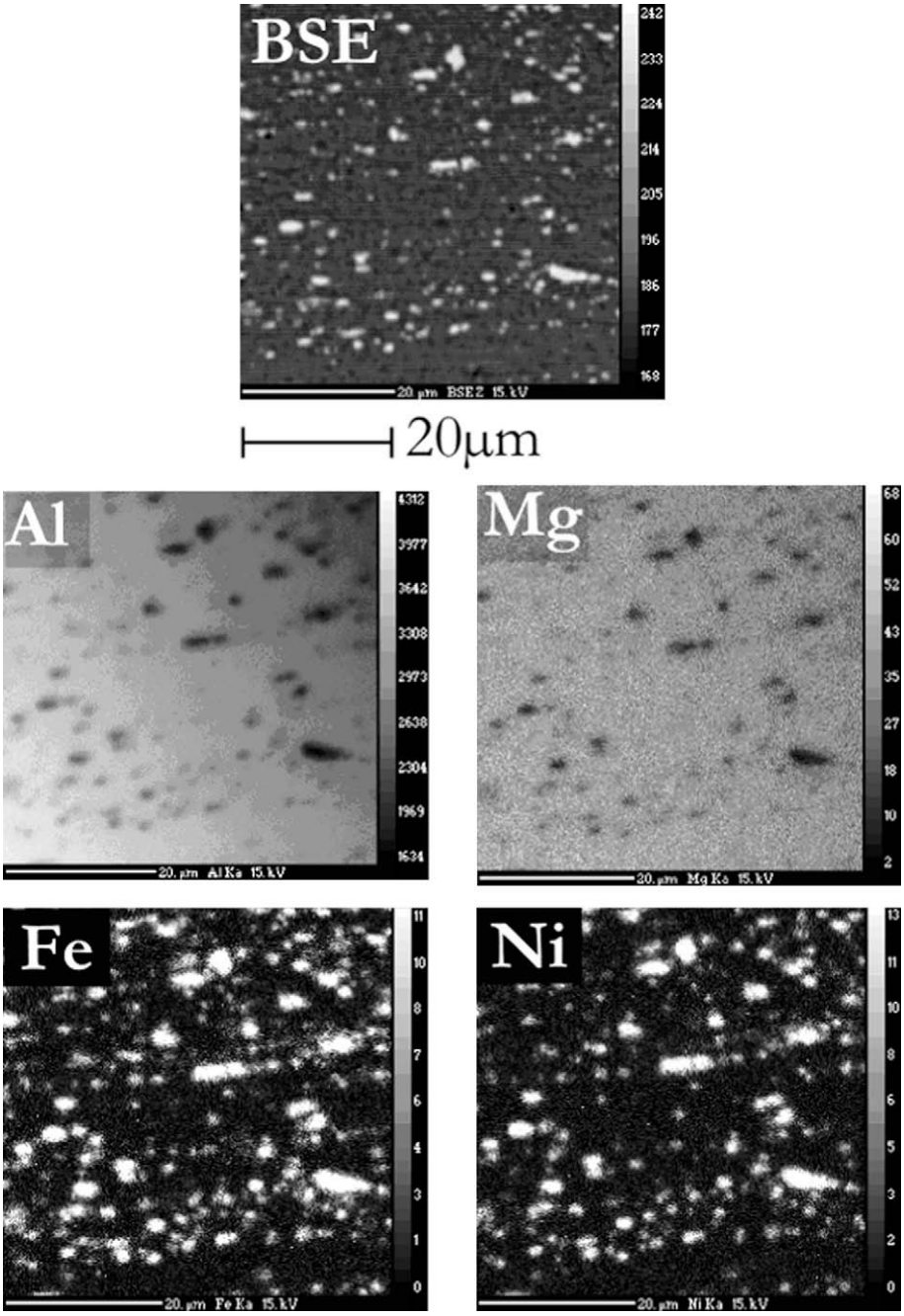

Fig. 2. BSE micrograph and Al Kα, Mg Kα, Fe Kα, and Ni Kα X-ray maps of the AlFeNi alloy.

formation of such cracks [12,13]. They can appear during the hot embedding or the mechanical polishing of the altered sample. But growth stresses or thermal stresses could be also responsible for the formation of such cracks. Indeed, differences of specific volumes (Pilling–Bedworth ratio [14] between 1.99 and 3.22) or epitaxial relations between the metallic matrix and the oxide can induce stresses during the oxide growth or thermal stresses can also appear during the cooling of the autoclave.

Secondly, the inner layer, close to the metal is dense and amorphous (XRD, μ-Raman spectroscopy and TEM results). Its structure is based on a mixture of aluminium and magnesium oxides or hydroxides (EPMA and EDS results). At 250 °C, magnesium diffuses in the metallic matrix to be oxidized inside this layer as shown by EPMA profiles [15] (Fig. 6). However, at 70 °C and 165 °C, diffusion is too low to be observed with EPMA measurements. The diffusion of magnesium can be explained by its higher affinity for oxygen compared to aluminium [16], which explains that it is firstly oxidized. Al_9FeNi precipitates are not affected by the oxidation (Fig. 7) process since iron and nickel potentials [16] are higher than that of magnesium and aluminium.

Thirdly, the outer layer, in contact with the water, is composed of pure aluminium hydroxide crystals (Fig. 8). There is no more trace of alloying element. Depending on the temperature of the leaching test, the thermodynamically stabilized crystalline phase was found to be different [17–19]: at 70 °C, bayerite $Al(OH)_3$ was identified while at 165 °C and 250 °C, boehmite AlOOH is stable, as confirmed from XRD and μ-Raman spectroscopy. Moreover, the morphology and size of the crystals appear to be strongly

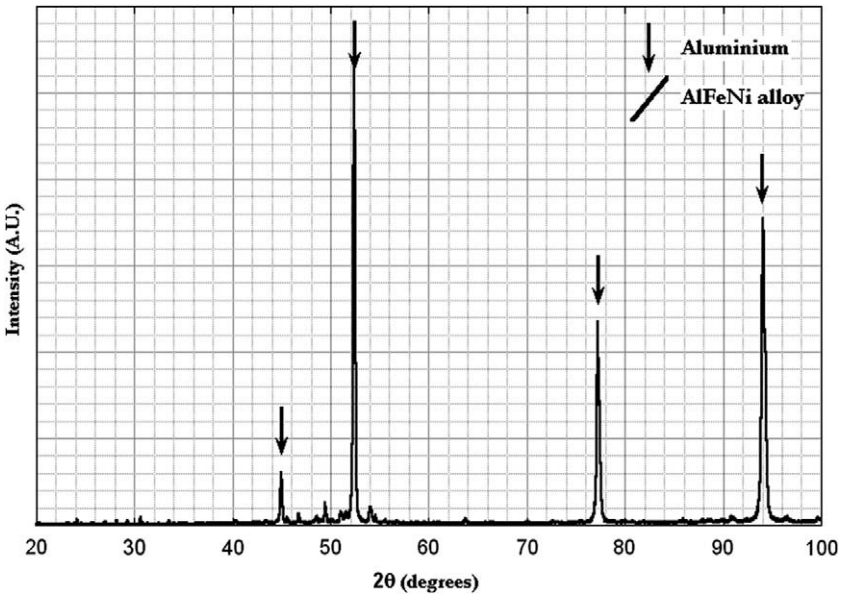

Fig. 3. XRD diagram of AlFeNi alloy and reference pattern PDF file # 089-2837 for aluminium.

dependent on the leaching conditions: temperature, dissolved species concentrations, water composition ... A common feature is that the crystal size increases from the inner to the outer interface.

Between the amorphous layer and the crystals formed at the external interface, an intermediate zone was observed. This zone is divided in two layers (Figs. 8 and 9): the first one, close to the amorphous oxide, is composed with small longitudinal crystals, perpendicular to the interface. Over these oriented crystals, lots of other small crystals grow randomly as a support for the larger crystals of the external layer. According to the fractography (Fig. 8) both parts do not exhibit the same mechanical behaviour. Fracture within the oriented crystals follows the same direction than that observed in the amorphous layer, and follows crystal faces for disordered ones. This is an indication that each one takes part to the inner or to the outer oxide layer. Another indication is the presence of Al_9FeNi precipitates in this intermediate zone (Fig. 5 dotted line encircled) that will be described in the following sections.

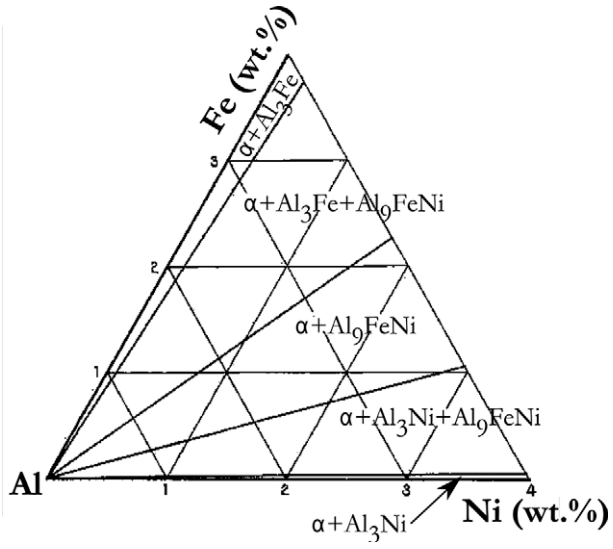

Fig. 4. Ternary diagram of the Al–Fe–Ni system at 600 °C [8].

3.3. Corrosion kinetic of the AlFeNi alloy

To follow the kinetic of corrosion of the AlFeNi alloy, various indicators have been compared. As usually reported in such studies dealing with corrosion, the recording of weight gain was used; but due to the duplex structure of the corrosion film, thickness measurements of each part of the layer were also performed. To get the kinetic curve, each point results from one experiment.

Following this protocol, there is no impact of the experiment shut down period on the kinetic. Indeed the direct comparison between two experiments performed in the same conditions (250 °C in a titanium autoclave during 34 days) has demonstrated that interruptions every 7 days with water renewals to weight the samples for an ongoing experimentation have a strong impact on the

Table 2
Comparison of the grain surfaces between the different AlFeNi rolled sheets.

Cold worked hardening level (%)	Annealed temper	Average surface (in mm^2)	Standard error (in mm^2)	Grain morphology
16	Cold worked	4.4	4.6	Anisotropic grains, oriented by the rolling direction
16	Annealed 2h30 at 425 °C	0.8	0.9	Middle size grains, around isotropic ones
20	Cold worked	2.8	2.4	Very anisotropic structure with grains stretching in the rolling direction
20	Annealed 2h30 at 425 °C	0.3	0.4	Very little equiaxed grains

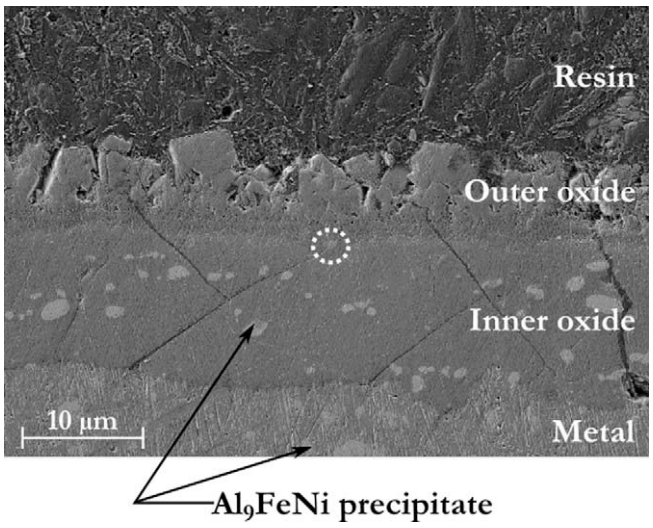

Fig. 5. SEM micrograph of corrosion products (13 days, 250 °C). At least two layers are visible in the oxide film.

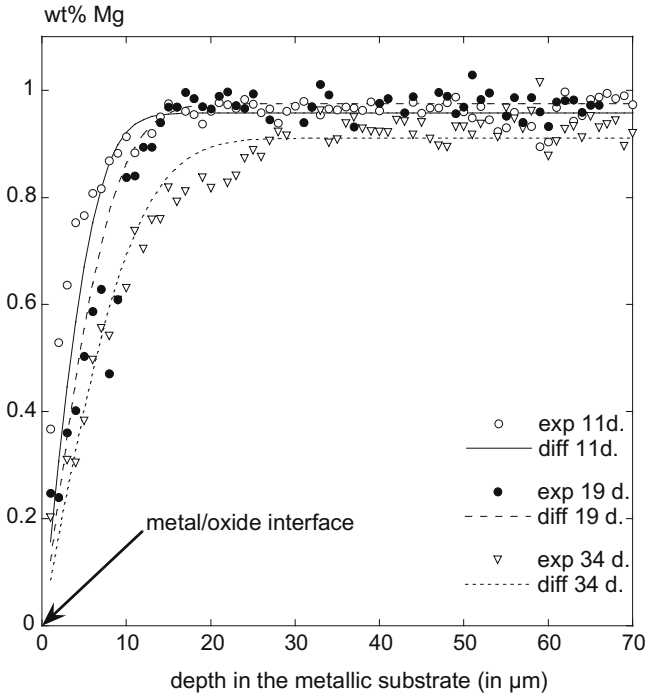

Fig. 6. Experimental (250 °C) and calculated magnesium profiles in α matrix at the interface with the oxide product. To calculate magnesium diffusion profiles, the following expression has been used: $c(x,t) = c_0.erf(\frac{x}{2\sqrt{Dt}})$ with $D = D_0.\exp(-\frac{Q}{RT})$ where $D_0 = 1.24\ cm^2\ s^{-1}$ and $Q = 130.33\ kJ\ mol^{-1}$. x and t correspond to the distance from the metal/oxide interface (in meter) and the duration of diffusion (in seconds). c_0 is the specified magnesium content (in wt%) in the matrix [15]. In the captions, "exp" is used for the experimental measurements by EPMA on samples oxidized for 11, 19 or 34 days, while "diff" designs the calculated diffusion profiles.

corrosion kinetic. Without any interruption and water renewal during 34 days, inner and outer oxide layers are twice thicker than in performing water renewal (Table 3). Moreover the weight gain is only 26% higher. And the consumed alloy's thickness evaluated through the weight loss after oxide desquamation, is 23% higher. According to the followed corrosion protocol, kinetic but also oxides densities are modified as demonstrated by the geometrical material balance (Fig. 10). Indeed, in stopped experimentation case, the inner oxide is denser than the metal since the interface between amorphous and crystalline oxide layers is located below the initial position of metallic surface. During non-interrupted corrosion experiments, this inner/outer oxide interface is located beyond the initial metal surface, as a proof that the oxide becomes less dense than the AlFeNi alloy.

Using the one point – one experimentation procedure, we got the kinetic of corrosion for the AlFeNi alloy at 250 °C in autoclave. The data obtained to reach the corrosion kinetic curves reported (Table 4, Fig. 11) appeared difficult to be fit correctly. Nevertheless, the weight gain is following a trend close to a parabolic law.

3.4. Characterization and oxide growth mechanism

In order to elucidate the mechanisms of growth of oxide scale, complementary experiments were developed. Gold has been vaporized on the polished metal surface before insertion in the autoclave. Gold position on metallurgical cross section enables to detect the initial location of the metal surface. A transverse observation of the corroded sample (Fig. 12) shows that the gold layer is exactly in the middle of the intermediate zone at the interface between the amorphous and the crystalline layers. As an usual method to determine the corrosion mechanism, this labelling protocol clearly demonstrates the mixed growth mechanism of the corrosion product [20–22]. The inner amorphous film forms itself by an inward movement of anions (or associated defects), whereas the outgrowth of the crystalline film results from an outward movement of metallic cations (or associated defects). The ingrowth of the amorphous layer also explains the presence of the intermetallic precipitates in its structure.

As previously explained, the grains morphology in the external layer is strongly dependent on the environmental conditions (dissolved species concentrations...) and particularly on temperature. Moreover, the stabilized external crystalline phase changes with temperature. Indeed, while bayerite is the stable form at 70 °C, boehmite is obtained for temperatures above 165 °C. At 165 °C boehmite crystals are elongated and perpendicular to the surface (around 1 μm depth). At 250 °C they are much larger and equiaxed (between 2.5 and 5 μm for cubic length). So the formation mechanism of the external layer is dependent on temperature.

Solid Nuclear Magnetic Resonance (NMR) has been performed on oxide powder, showing two kinds of environments for the aluminium atoms: octahedral and tetrahedral coordination. Well-known in all aluminium oxides and hydroxides, the six-fold coordination is the main one observed in our corrosion product, whereas the four-fold aluminium atoms are in minority. According to the literature, this coordination was only observed in a polycation as a precursor for aluminium oxyhydroxide and hydroxide crystals by condensation of aqueous aluminium species [23].

On another side, aqueous analysis shows that magnesium is dissolved in the solution, while there is no evidence of aluminium in solution. This is consistent with the relative solubilities of aluminium and magnesium oxides and hydroxides in these temperatures and pH ranges [24,25]. In these aqueous conditions, magnesium is soluble in water, whereas aluminium usually precipitates. The corrosion products release (particularly of magnesium) induces modifications of the water conductivity: from 1 $\mu S\ cm^{-1}$ to an average value of $7.2 \pm 5.9\ \mu S\ cm^{-1}$. On other side, the pH increases from 6.9 to 7.4 ± 0.3, what is consistent with the magnesium concentrations. The specific precipitation of aluminium explains the plain composition of the crystalline layer. On other side, pH influence has been controlled by corrosion experimentations in an aqueous media with nitric acid or sodium hydroxide additions. As shown in Fig. 13, the weight gain decreases with the pH increase of the corrosive solution.

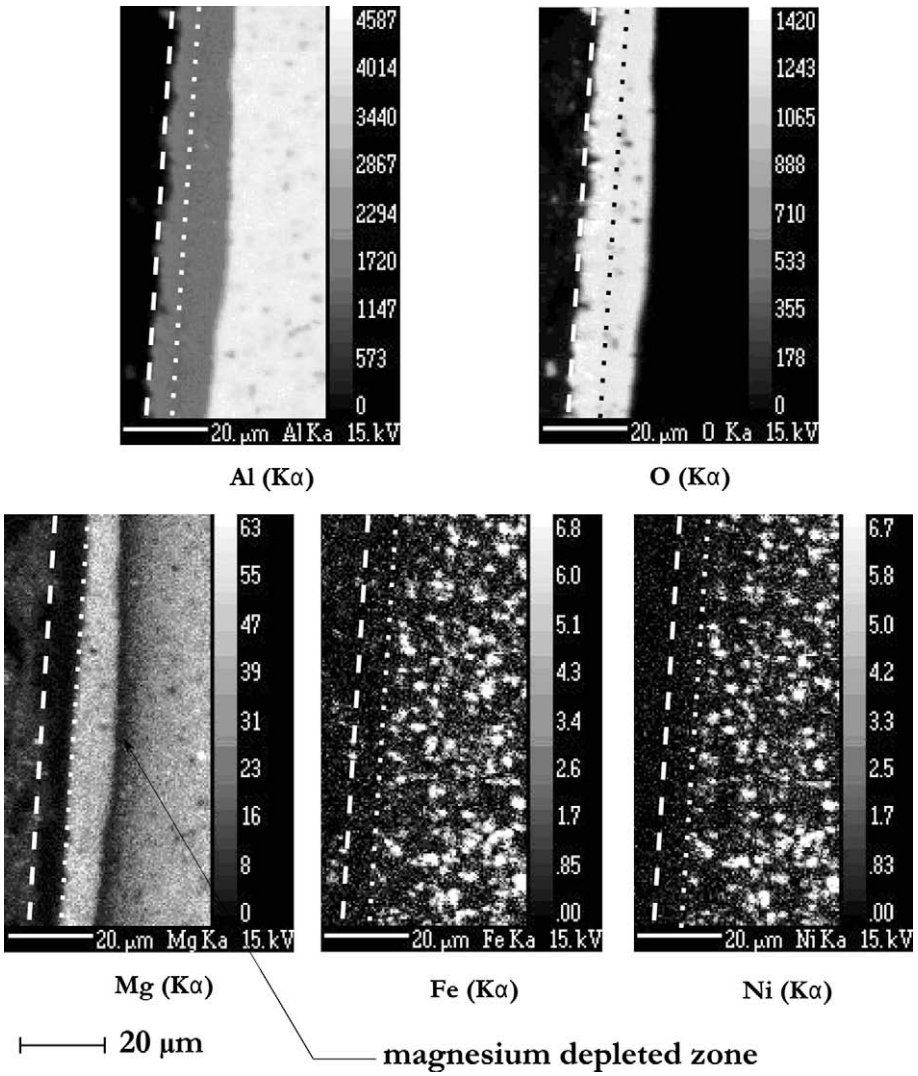

Fig. 7. Al Kα, O Kα, Mg Kα, Fe Kα, and Ni Kα X-ray maps of the corrosion product on AlFeNi plates after 42 days in an autoclave at 250 °C. Dotted lines symbolize the interface between inner and outer oxide layers, dashed lines the interface between corrosion product and resin.

Moreover, since the aluminium is the main compound of the AlFeNi alloy, weight gain is not a good indicator for the oxide thicknesses, but traduces with a good accuracy the degradation amplitude. As previously explained for the kinetic protocol comparison, it seems that the corrosion depends on the aqueous conditions: water renewal, pH, temperature. These parameters change also the oxide properties like, for example, its porosity or its density. According to the chemical equilibrium for the oxide formation in acidic or basic conditions, it suggests that the decrease of protons promotes hydroxide formation with consumption of metallic cations:

$$Al^{3+}_{(aq)} + 2H_2O \rightleftharpoons AlOOH_{(s)} + 3H^+ \quad (1)$$

$$Al^{3+}_{(aq)} + 3HO^- \rightleftharpoons AlOOH_{(s)} + H_2O \quad (2)$$

All these observations led us to propose the following growth mechanism. On the one side oxidative species (not identified at this time: HO^- or O^{2-}) diffuse through the amorphous oxide to reach the metal/oxide interface where the oxidation/reduction reaction takes place with formation of the magnesium and aluminium oxides and hydroxides mixture. On the other side, metallic cations (Al^{3+} and Mg^{2+}) diffuse from the metallic matrix to the inner/outer oxides interface. Certainly at this interface, cations are solubilised in water and their quantities depend on the pH on the oxidative solution. Since the diffusion of the metallic cations is controlled by the concentration gradient between the metal/oxide interface and the solution, pH can control the corrosion process. Due to its low solubility, aluminium immediately precipitates to form pure aluminium hydroxide crystals, while magnesium diffuses in this layer up to the bulk solution. The precipitation kinetic changes with aqueous conditions (temperature, pH, species concentrations...), which can explain the differences, observed in the crystals morphologies. At low temperature, precipitation kinetic is accelerated due to the lower aluminium solubility. So nucleation of new crystals is more rapid than the growth of those already formed, which leads to the multiplication of small crystals [23].

4. Dissolution experiments at 70 °C

In order to confirm the growth mechanism proposed above, some experiments in an open-circulation autoclave were developed at 70 °C (Fig. 14). In order to quantify the dissolution kinetic during the corrosion process, two leaching flow rates were used

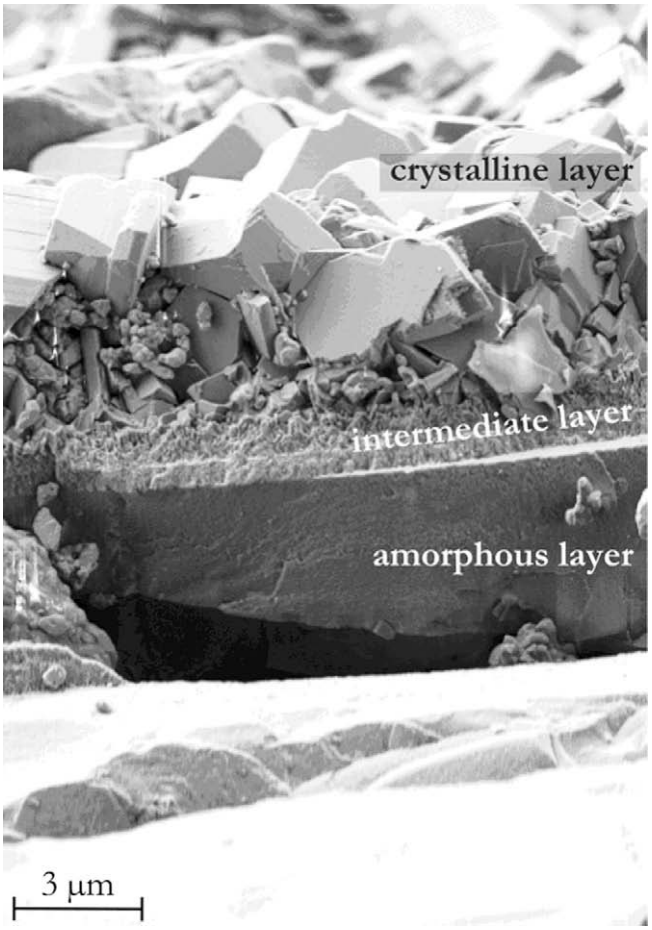

Fig. 8. Fractography of the oxide scale obtained after 13 days in an autoclave at 250 °C.

(100 and 200 mL h^{-1}, which corresponds to 4 and 8 complete renewals of the leaching solution per hour, respectively). The metallic samples were first polished before their introduction in the device. Many withdrawals have been bottled and then analyzed by ICP-AES to quantify the aluminium and magnesium concentrations in water. The normalized leachings were calculated in order to evaluate the dissolution rate of the material according to the following equation [26,27]:

$$N_i(t+\Delta t) = \frac{c_i(t)\cdot d\cdot \Delta t}{S\cdot f_i} + N_i(t)$$

With N_i, the normalized leaching for element "*i*" (in µg mm^{-2}), *t*, the cumulative leaching time (in hours), $c_i(t)$, the concentration of the element "*i*" determined by ICP-AES (in µg L^{-1}), *d*, the water flow rate (in L h^{-1}), Δt, the time interval between two withdrawals (in hours), *S*, the sample surface in contact with the solution (in mm^2) and f_i, the mass ratio for the element "*i*" in the material.

From SEM observations, the presence of the crystalline layer is confirmed, even for the highest flow rate. That demonstrates the importance of the interfacial phenomena in this system. Indeed, considering the aluminium concentration in the bulk water, the precipitation should not have occurred. The crystals formation is so associated to the saturation in the Helmotz layer by the aluminium species concentrations at the solid/solution interface.

According to levels measured by ICP-AES, the concentration of magnesium in solution is found to be three decades higher than that of aluminium, while aluminium is the main component of the AlFeNi alloy. That clearly underlines that aluminium is retained during the dissolution scheme. Moreover, two behaviours are observed on the curves devoted to the evolution of the mass loss during the leaching experiments (Fig. 15). During the first 3 h of leaching, the dissolution rate follows a sigmoïdal curve associated to the formation of oxide film at the solid/liquid interface. For

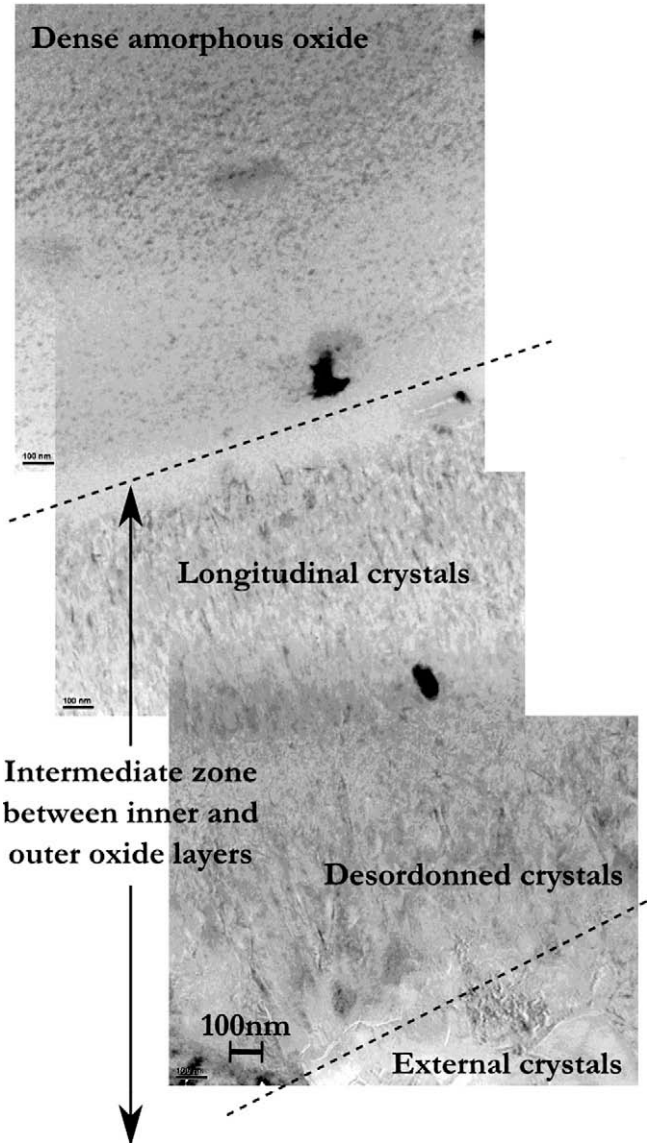

Fig. 9. TEM micrograph of the amorphous/crystalline layers interface in a corrosion product after 13 days in an autoclave at 250 °C.

Table 3
Comparison of the corrosion procedures at 250 °C in autoclave.

Corrosion protocol	Mean inner layer thickness (in µm)	Mean outer layer thickness (in µm)	Weight gain (in mg dm^{-2})	Lost metal thickness after oxide desquamation (in µm)
Real kinetic without interruption	24.0 ± 3.5	13.1 ± 2.2	329 ± 20	20.5 ± 6
With interruptions procedure	11.6 ± 1.0	6.1 ± 1.2	260 ± 16	16.6 ± 5

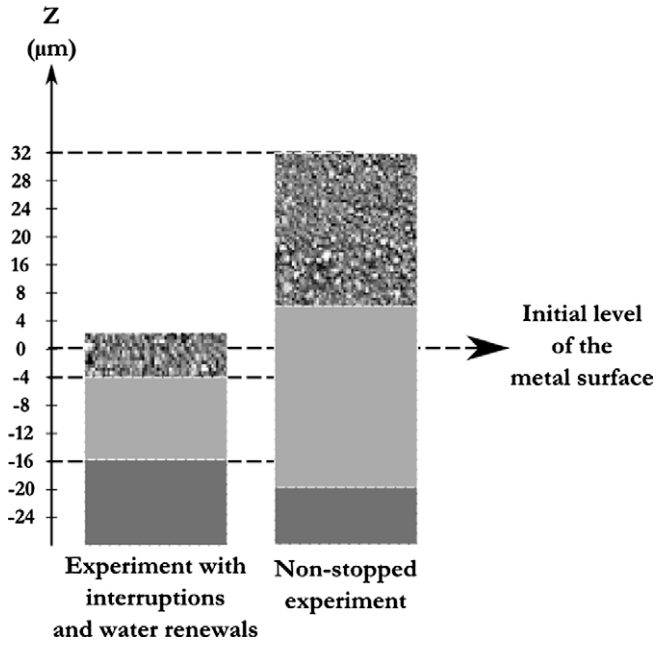

Fig. 10. Geometrical material balance depending on the used corrosion procedure, demonstrating the impact of the interruptions and water renewals on the corrosion kinetic.

longer leaching times, the magnesium and aluminium releases can be fitted with parabolic laws (dotted lines). This suggests that the leaching kinetic is controlled by diffusion phenomena. Moreover, considering that magnesium is a good tracer of the material dissolution (absence of precipitation), it seems that this diffusion process is close to be linearly dependent on the water flow rate (a two times higher flow rate leading to a twice more important release in magnesium) (Fig. 16).

5. Post-irradiation exams of AlFeNi cladding: corrosion behaviour in reactor

In order to qualify the JHR fuel plates, CEA ordered an irradiation of U_3Si_2 fuel plates in the Belgian BR2 reactor (SCK•CEN) at Mol (average heat flux 256 W cm^{-2} – average burnup 1.3×10^{21} fissions cm^{-3} meat). After three irradiation cycles of respectively 22.2, 20.5, and 26.1 days, no change in the alloy microstructure was reported on the AlFeNi cladding.

The post-irradiation exams [28] (optical micrography, SEM, XRD and EPMA) performed either on the cladding or on the corrosion layer show the formation of a corrosion product (Fig. 17) rather different from the corrosion product observed in static conditions.

The removed oxide powder was characterized through XRD [28], showing two aluminium constitutive hydroxides: boehmite AlOOH, on the one hand and bayerite $Al(OH)_3$, on the other hand.

Table 4
Kinetic study of the corrosion of the AlFeNi alloy in static autoclave at 250 °C.

Exposure time (in days)	Inner layer (in μm)	Intermediate layer (in μm)	Outer layer (in μm)	Total corrosion film (in μm)	Gain of mass (in μg/mm^2)
5.1	6.2 ± 1.0	0.9 ± 0.2	2.6 ± 0.5	9.8 ± 1.7	11.5 ± 2.3
10.7	13.6 ± 1.2	1.7 ± 0.4	7.1 ± 1.0	22.5 ± 2.6	15.4 ± 3.1
12.7	12.2 ± 1.2	1.5 ± 0.4	4.9 ± 1.1	18.6 ± 2.7	15.3 ± 3.1
14.0	18.3 ± 2.6	3.9 ± 1.3	7.5 ± 1.7	29.7 ± 5.6	21.1 ± 4.2
26.0	15.6 ± 1.2	2.8 ± 0.8	6.5 ± 1.2	24.9 ± 3.2	23.0 ± 4.6
51.8	15.6 ± 1.3	1.9 ± 0.5	7.2 ± 1.4	24.8 ± 3.2	29.4 ± 5.9

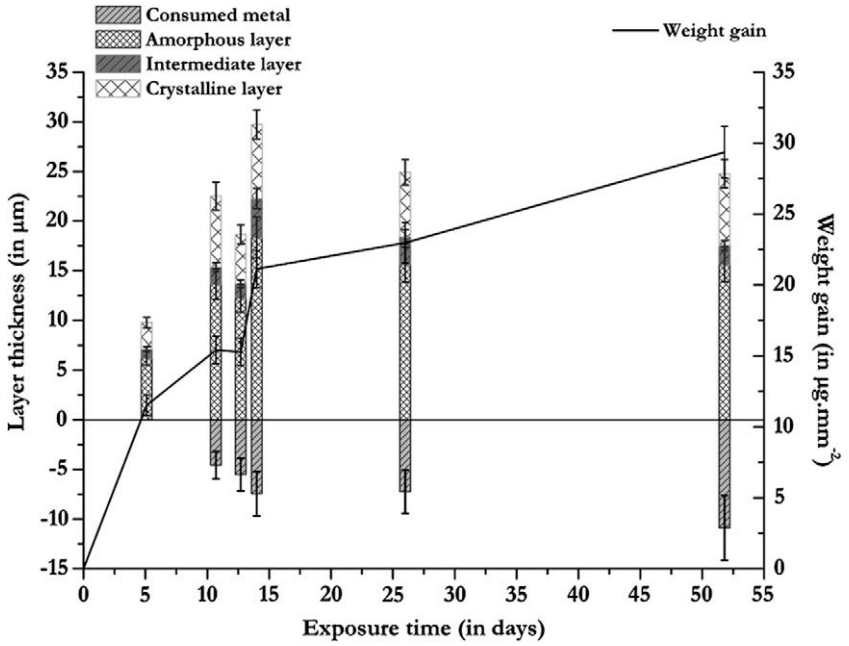

Fig. 11. Corrosion of AlFeNi alloy at 250 °C in autoclave measured by weight gain and oxide layer thickness determination.

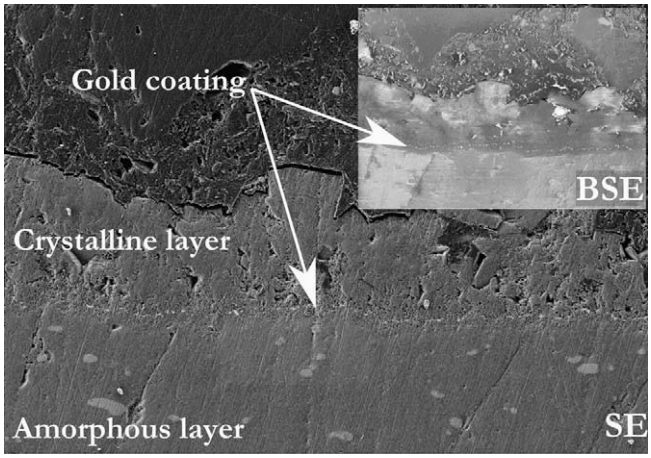

Fig. 12. SEM micrograph of the corrosion product with gold layer at the interface between amorphous and crystalline layer (testing conditions: 34 days at 250 °C in autoclave).

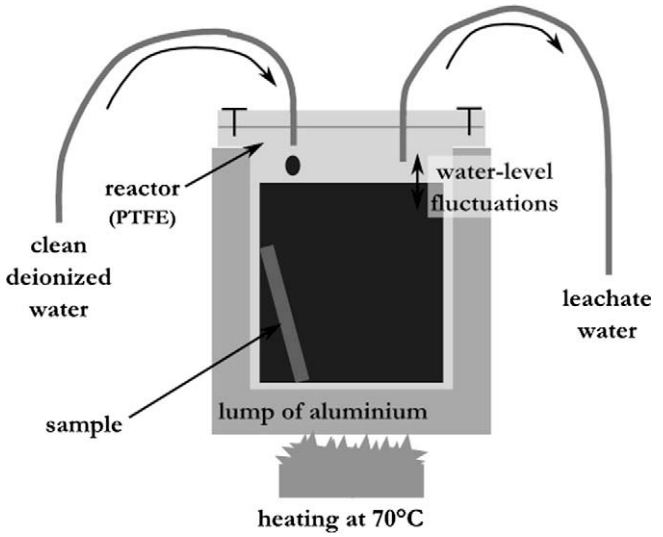

Fig. 14. Leaching device used to follow the releasing kinetic of corrosion products. The teflon reactor is continuously filled with hot deionized water. On the other side, the leachate water is continuously pumped out and withdrawals are analyzed by ICP-AES.

Both have been observed in autoclaves as outer crystals, at 165–250 °C and 70 °C, respectively. Their simultaneous presence in the oxide powder is certainly linked to the variation of temperatures over the cladding between the center and the extremities of the fuel plate. According to the calculations developed on this fuel plate, the cladding temperature reached 144 °C at the hottest point, whereas the coldest one was submitted to 59 °C. Moreover the water temperature in the canals of the fuel assembly can increase from 35 °C to 158 °C. These calculated temperatures were thus sufficient to explain the formation of the two hydroxides observed, depending on the spatial position on the clad and on the local temperatures.

As in autoclaves, the corrosion layer shows a lot of cracks. Nevertheless, the number and size of these cracks seem to be higher over the fuel plates than over the inert specimens. As suggested in [28], this difference can be interpreted as a consequence of dehydration of the hydroxide structure. It could also result from strong thermal stresses associated to variations of thermal gradient through the cladding. Whereas the specimens are directly exposed to the regulated bulk temperature in autoclave, the fuel plate is subject to many temperatures modifications in the reactor. All these variations change continuously the thermal induced stresses in the fuel cladding and in its oxide.

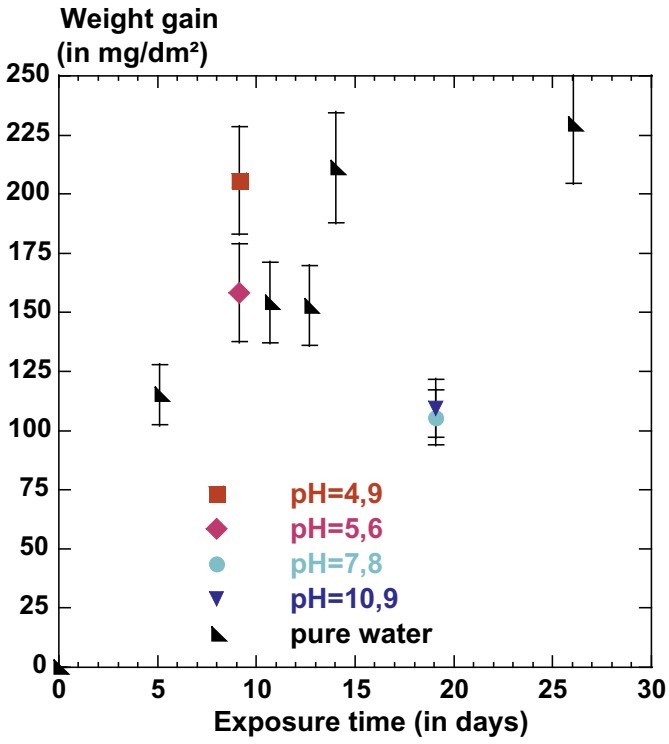

Fig. 13. pH influence on the weight gain kinetic of AlFeNi alloy in aqueous media. Nitric acid or sodium hydroxide were used to adjust the pH.

As shown in Fig. 17, the corrosion product keeps a duplex structure, with a layer showing the Al_9FeNi precipitates close to the metal and an outer layer without (or less visible) intermetallic phase, which seems to be amorphous. Moreover, the interface between both parts of the oxide layer is not so plain than in autoclave. According to the EPMA profiles in the irradiated clad, the chemical composition of the external oxide layer is also rich in alloying elements. Considering the profile of the magnesium content, the visible oxide contains a decreasing content of magnesium. That is not in accordance with the previous observations on the corrosion products obtained in autoclave: while the amorphous layer was enriched in magnesium compared to the metallic substrate, the crystalline layer was pure aluminium hydroxide without any traces of magnesium. The corrosion layer in reactor is thus neither the previously identified "outer" layer, but nor the "inner" layer. One interpretation of these observations is that the crystalline layer does not exist in the reactor. The part of the oxide where precipitates are not visible could be a degraded or crystallized part of the inner layer, defined previously as the "intermediate" layer, which could also explain why the magnesium content decreases trough this layer.

In the BR2 reactor, the corrosion conditions are quite different from that obtained in autoclave or in the leaching device. First, the water flow rate is very high in the reactor ($\sim$11 m s^{-1}), which strongly modifies the hydraulic conditions. Second, radiolysis of the water occurs under the neutron flux. Free radicals and others species are able to modify the corrosion conditions: more oxidative water, different pH range. Particularly at the interface between porous alumina and water, irradiation induces a strong local production of dihydrogen, through water radiolysis and irradiation of hydrated materials (homolytic breaking of the O–H bond). Third,

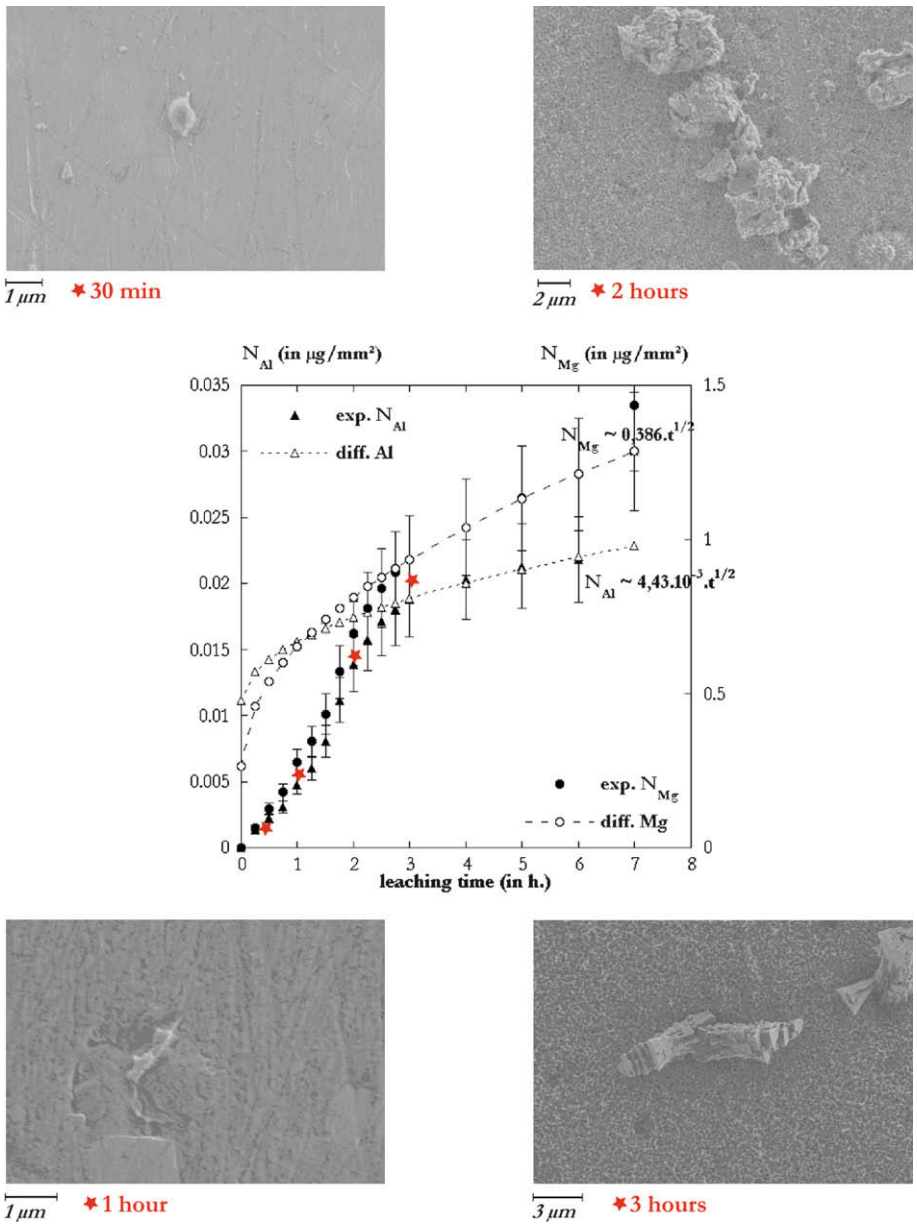

Fig. 15. Variation of the cumulative normalized leachings N_{Al} and N_{Mg} versus leaching time at 70 °C (flow rate of 200 mL h^{-1}). The associated micrographs at 30 min, 1 h., 2 h. and 3 h. show the link between the modification of the dissolution kinetic and the development of an oxide scale over the metallic surface. Experimental data can be fitted with a "parabolic" law from 3 h. of experimentation suggesting a diffusion process as kinetic control step.

solid diffusion is accelerated under irradiation. Indeed under irradiation by neutrons, formation of positives holes, electrons and vacancies occurs in the oxide and in the metal. All those microscopic defects can enhance the atomic displacements and accelerate the diffusion phenomena for the species implicated in the corrosion process. Irradiation can also inhibit the crystallization of aluminium hydroxide on the amorphous oxide surface. All these differences can explain this new oxide morphology. But the kinetic is also strongly accelerated in the reactor. At the hottest point of the fuel plate (~160 °C), the oxide thickness has reached 50 μm after 69 days compared to the 5 μm (average thickness) formed after 34 days of exposure in autoclave at 165 °C.

6. Conclusions

The AlFeNi aluminium alloy corresponds to the fcc α matrix of aluminium in which magnesium is substituted to aluminium. In this solid solution, two kinds of intermetallic phases are present. Al_9FeNi and chromium rich precipitates are homogenously dispersed in the matrix. Their size (1 μm and 200 nm of diameter respectively) and dispersion are not dependent on the metallurgical temper. But the metallic grain size and morphology are strongly modified according to the strain hardening and the annealing heat treatment.

The corrosion product on AlFeNi alloy in water exhibits a duplex structure, with an amorphous oxide layer close to the metal and a crystalline one in contact with the solution. The degradation process is composed of at least three steps. The first one corresponds to the oxidation/reduction of aluminium and magnesium at the metal/oxide interface. An amorphous oxide results from the reaction and grows into the metal. Oxidative species (HO^- or O^{2-}) diffuse from the intermediate interface between amorphous and crystalline layers to reach the metallic surface. Simultaneously, aluminium and magnesium cations diffuse through this amor-

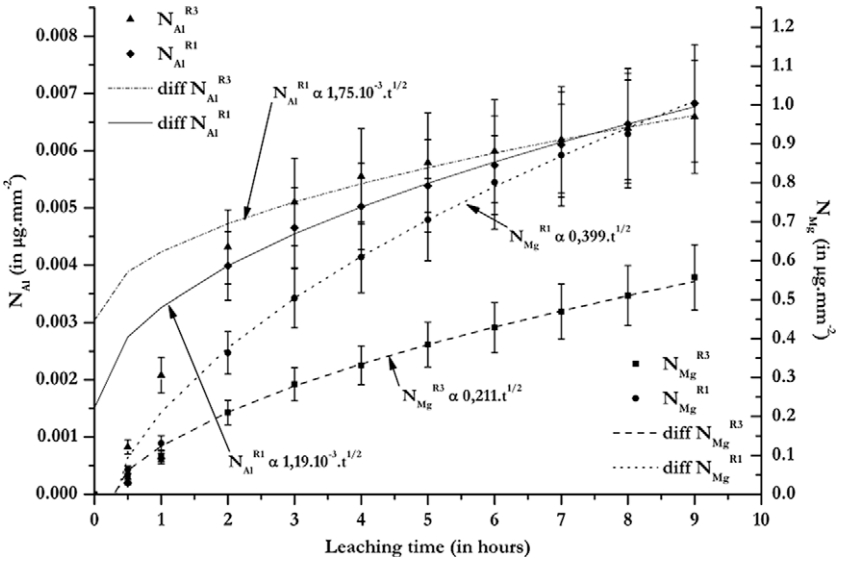

Fig. 16. Variation of the cumulative and normalized leaching N_{Al} and N_{Mg} versus leaching time at 70 °C for two rates of 100 mL h^{-1} and 200 mL h^{-1} (R3 and R1 respectively). From 3 h. experimental data have been fitted with "parabolic" laws.

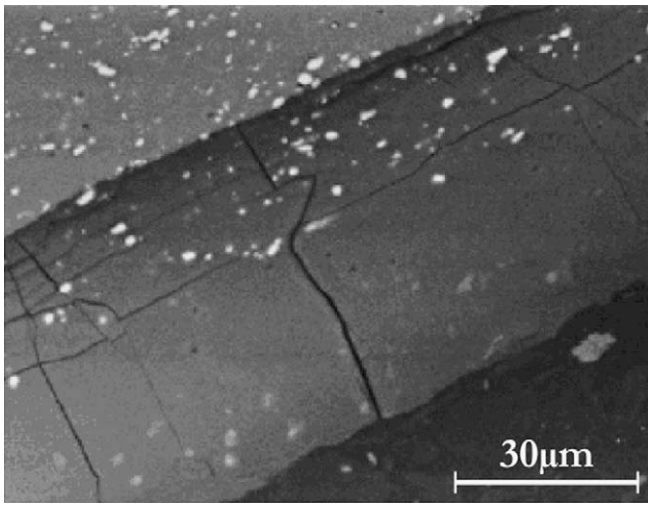

Fig. 17. Backscattered electron image of the oxide scale on the AlFeNi cladding of the U_3Si_2 fuel plate during SHARE irradiation [28].

phous layer. At the external interface of this layer (amorphous/crystalline layers), aluminium and magnesium cations are released in the bulk solution. Due to its low solubility, aluminium precipitates specifically by condensation of polycations. These polycations are the precursors for the formation of hydroxide crystals constitutive of the outer oxide layer.

According to the magnesium behaviour during the leaching tests at 70 °C, the dissolution rate seems to be affected by cationic diffusion inside the amorphous layer and increases with the water velocity. It would be strongly interesting to perform the same kind of dissolution measurements at 250 °C as a confirmation of the diffusion-controlling step through the amorphous layer. Moreover corrosion tests performed with and without interruptions for water renewal showed that the density of the amorphous layer varies with the thermal-hydraulic conditions. This has a strong impact on the corrosion rate which decreases when the amorphous layer is denser. It is suggested that this density increase could be related to temperature cycling. Further tests should be performed to confirm this assumption.

In nuclear reactor, the corrosion product is thicker than in autoclave, even at a lower temperature. The corrosion kinetic is thus strongly accelerated under dynamic flow and irradiation conditions. More than the kinetic of corrosion, the morphology of the corrosion product seems to be modified since the oxide scale seems not to show a duplex structure anymore. Various reasons associated to thermal-hydraulic conditions or water radiolysis could explain the formation of a new degradation structure, but complete analyses are required to complete the description of the oxide layer and select the right corrosion process in these new conditions.

By understanding completely the corrosion mechanisms of AlFeNi aluminium alloy, it will be possible to build a physical correlation between oxide thickness and staying time in reactor. With this aim, the identification of the oxidative species diffusing through the inner layer and of associated reaction constants will be necessary. Quantitative evaluations of the respective parameters impact (temperature, pH, ionic concentrations...) will be presented in a forthcoming publication.

Acknowledgements

The authors thank each person who is taking part in this work for the analyses, for the experimentations, for the interpretations from CEA Saclay (DEN/DMN and DEN/DPC), from CNRS, from Orsay's Nuclear Physics Institute (IPNO/IN2P3, N. Barré) and from SCK•CEN. They thank also M. Audoit from SERMA Technologies for performing the TEM analyses.

References

[1] J.C. Griess, H.C. Savage, J.L. English, Effect of Heat Flux on the Corrosion of Aluminium by Water. Part IV. Tests Relative to the Advanced Test Reactor and Correlation with Previous Results, ORNL-3541, Oak Ridge National Laboratory, 1964.
[2] R.S. Ondrejcin, Evaluation of Mark-22 Cladding, DPST-83-324, Savannah River Laboratory, 1983.
[3] R.E. Pawel, D.K. Felde, M.T. McFee, The Development of an improved correlation for corrosion product growth on aluminium alloy fuel cladding for the advanced neutron source, in: Sixth International Symposium on Environmental Degradation of Materials in Nuclear Power Systems–Water Reactors, 1993.
[4] S.J. Pawel, D.K. Felde, R.E. Pawel, Influence of Coolant pH on Corrosion of 6061 Aluminium under Reactor Heat Transfer Conditions, ORNL/TM-13083, Oak Ridge National Laboratory, 1995.

[5] P.-P. Malgouyres, Modélisation ANS II avec terme pH – Application à des irradiations de plaques combustibles HFIR, technical report NT DEC/S3C/03-149, CEA-Cadarache, 2003.
[6] Y.S. Kim, G.L. Hofman, A.B. Robinson, J.L. Snelgrove, N. Hanan, J. Nucl. Mater. 378 (2008) 220.
[7] J.E. Draley, W.E. Ruther, Corrosion resistant aluminum above 200 °C, report no. 5430, ANL, 1955.
[8] H. Coriou, L. Grall, J. Hure, A. Roux, Alliages d'aluminium contenant du fer et du nickel. Influence de la structure et de la teneur sur la résistance à la corrosion par l'eau à haute température, report no. 1193, CEA-Saclay, 1959.
[9] C. Vargel, Propriétés générales de l'aluminium et de ses alliages, Techniques de l'Ingénieur M4661.
[10] R. Develay, Traitements thermiques des alliages d'aluminium, Techniques de l'Ingénieur M1290.
[11] Heat treating of aluminum alloys, ASM Handbook, Heat Treating, ASM, vol. 4, 1991, p. 841.
[12] M. Schütze, Protective Oxide Scales and Their Breakdown, Wiley, 1991.
[13] A.M. Huntz-Aubriot, B. Pieraggi, Oxydation des Matériaux Métalliques, Hermes Science, Paris, 2003.
[14] N.B. Pilling, R.E. Bedworth, J. Inst, Metals 1 (1923) 529.
[15] H.P.J. Leighly, A. Alam, J. Phys. F Metal Phys. 14 (1984) 1573.
[16] M. Pourbaix, Atlas of Electrochemical Equilibria in Aqueous Solutions, Pergamon, 1966.
[17] K. Wefers, C. Misra, Oxides and Hydroxides of aluminum, Alcoa Technical Paper no. 19, revised, Alcoa Laboratories, 1987.
[18] R.S. Alwitt, The aluminium–water system, Oxides and Oxide films, vol. 4, Marcel Dekker, New-York/Basel, 1976, p. 169 (Chapter 3).
[19] C. Vargel, Corrosion de l'aluminium, Dunod, 1999.
[20] L. Pfeil, J. Iron Steel Inst. 199 (1929) 501.
[21] L. Pfeil, J. Iron Steel Inst. 183 (1931) 237.
[22] P. Sarrazin, A. Galerie, J. Fouletier, Les Mécanismes de la Corrosion Sèche, EDP Sciences, 2000, p. 68.
[23] J.-P. Jolivet, De la solution à l'oxyde. Condensation des cations en solution aqueuse – Chimie de surface des oxydes, InterEditions/CNRS Editions, 1994, p. 86.
[24] P. Benezeth, D.A. Palmer, D.J. Wesolowski, Geothermics 26 (4) (1997) 465.
[25] I. Lambert, A. Lefèvre, J. Montel, Solubility of magnesium hydroxide in aqueous solutions from 20 °C to 300 °C. Influence of chlorides, in: International CODATA Conference, Jachranka, Poland, 1982.
[26] G. Heisbourg, S. Hubert, N. Dacheux, J. Ritt, J. Nucl. Mater. 321 (2003) 141.
[27] N. Dacheux, N. Clavier, J. Ritt, J. Nucl. Mater. 349 (2006) 291.
[28] A. Leenaers, E. Koonen, Y. Parthoens, P. Lemoine, S. Van den Berghe, J. Nucl. Mater. 375 (2008) 243.